

## A theory for the Hadley cell descending and ascending edges throughout the annual cycle

SPENCER A. HILL,<sup>a,b</sup> SIMONA BORDONI,<sup>c,d</sup> AND JONATHAN L. MITCHELL<sup>e,f</sup>

<sup>a</sup> *Program in Atmospheric and Oceanic Sciences, Princeton University, Princeton, New Jersey*

<sup>b</sup> *Lamont-Doherty Earth Observatory, Columbia University, Palisades, New York*

<sup>c</sup> *Department of Civil, Environmental and Mechanical Engineering (DICAM), University of Trento, Trento, Italy*

<sup>d</sup> *Division of Geological and Planetary Sciences, California Institute of Technology, Pasadena, California*

<sup>e</sup> *Department of Atmospheric and Oceanic Sciences, University of California, Los Angeles*

<sup>f</sup> *Department of Earth, Planetary, and Space Sciences, University of California, Los Angeles*

**ABSTRACT:** We present a theory for the latitudinal extents of both Hadley cells throughout the annual cycle by combining our recent scaling for the ascending edge latitude (Hill et al. 2021) based on low-latitude supercriticality with the theory for the poleward, descending edge latitudes of Kang and Lu (2012) based on baroclinic instability and a uniform Rossby number ( $Ro$ ) within each cell’s upper branch. The resulting expressions for all three Hadley cell edges are predictive except for diagnosed values of  $Ro$  and two proportionality constants. Thermal inertia—which damps and lags the ascent latitude relative to the insolation—is accounted for semi-analytically through the Mitchell et al. (2014) model of an “effective” seasonal forcing cycle. Our theory, given empirically an additional  $\sim 1$ -month lag for the descending edge, captures the climatological annual cycle of the ascending and descending edges in an Earth-like simulation in an idealized aquaplanet general circulation model (GCM). In simulations in this and two other idealized GCMs with varied planetary rotation rate ( $\Omega$ ), the winter, descending edge of the solstitial, cross-equatorial Hadley cell scales approximately as  $\Omega^{-1/2}$  and the summer, ascending edge as  $\Omega^{-2/3}$ , both in accordance with our theory. Possible future refinements and tests of the theory are discussed.

### 1. Introduction

Climatologically over the annual cycle, the poleward, descending edges of the Hadley cells vary meridionally by  $\lesssim 5^\circ$  latitude about their annual-mean positions, considerably less than the  $\sim 15^\circ\text{S}$ – $15^\circ\text{N}$  range of the shared, ascending edge (c.f. Fig. 4 of Adam et al. 2016). These result in a pronounced seasonal cycle of zonal-mean rainfall in the deep tropics versus more consistently dry conditions in the subtropics. Regional hydrological deviations from the zonal average are pronounced—with for example intense Indian summer monsoon rainfall spanning roughly the same latitudes as the Sahara and Arabian deserts (Rodwell and Hoskins 1996)—nevertheless we focus on the zonal-mean dynamical problem, seeking a minimal explanation for the differing annual cycles of the Hadley cell descending and ascending edges (henceforth  $\varphi_d$  and  $\varphi_a$  respectively and formally defined below in terms of the mass overturning streamfunction).

For  $\varphi_d$ , our starting point is the theory of Kang and Lu (2012, henceforth KL12), whose own starting point is that of Held (2000, henceforth H00) for the annual-mean  $\varphi_d$  that assumes the Hadley cells terminate where their zonal wind profiles become baroclinically unstable. KL12 extend the H00 model in two key ways. First, they generalize from the annual mean to the annual cycle by accounting, albeit diagnostically, for off-equatorial  $\varphi_a$ . For angular-momentum-conserving (AMC) zonal winds as assumed

by H00, ascent off the equator results in less positive zonal winds at each latitude (Lindzen and Hou 1988) and thus to baroclinic instability onset occurring farther poleward than for equatorial ascent. All else equal, this would cause  $\varphi_d$  to be farther poleward in solstitial seasons when  $\varphi_a$  is farther off-equator than in equinoctial seasons. An example of this framework’s utility is Hilgenbrink and Hartmann (2018), who interpret changes in  $\varphi_d$  throughout the annual cycle caused by ocean heat transports in terms of changes in  $\varphi_a$ .

Second, KL12 relax the H00 assumption of strictly AMC winds by assuming that the Rossby number ( $Ro$ ) is uniform throughout each Hadley cell’s upper branch but not necessarily unity. Its formal definition follows below, but for now  $Ro$  is exactly unity for AMC winds and exactly zero if zonal winds themselves are zero, and KL12 derive an analytical expression for the meridional profile of zonal wind under uniform  $0 < Ro \leq 1$ . In simulations (Walker and Schneider 2006) and reanalysis data (Schneider 2006),  $Ro$  is regularly below unity and typically smaller in the equinoctial and summer cells than in the cross-equatorial winter cell (Bordoni and Schneider 2008; Schneider and Bordoni 2008). By diagnosing a bulk value of  $Ro$  for each cell and meteorological season in addition to  $\varphi_a$ , KL12 provide closed expressions for the northern and southern hemisphere descending edge latitudes in all four seasons.<sup>1</sup>

<sup>1</sup>Other authors also have considered a uniform  $Ro$  in the tropical upper troposphere. Becker et al. (1997) find that a uniform  $Ro = 0.5$  approximation (their Fig. 7 and Eq. 28) adequately captures the vorticity distribution in the descending branch of the winter Hadley cell in their

For  $\varphi_a$ , in Hill et al. (2021) we presented a scaling for  $\varphi_a$  by assuming that it is set by the meridional extent of supercritical radiative forcing in the summer hemisphere (the meaning of which we expand upon below). In essence, the present study simply replaces the diagnosed  $\varphi_a$  in the KL12 model with this predictive scaling. The one departure from Hill et al. (2021)—which implicitly treated thermal inertia as negligible by relating the seasonally varying  $\varphi_a$  to the contemporaneous insolation—is accounting for thermal inertia’s damping and delaying of the  $\varphi_a$  annual cycle via the analytical model of Mitchell et al. (2014). The result is a unified theory for  $\varphi_a$  and both hemispheres’  $\varphi_d$  with only two proportionality constants as well as Ro diagnosed (potentially with distinct Ro values required for each cell and season).

Separately, in general circulation model (GCM) simulations with differing planetary rotation rates ( $\Omega$ ) the solstitial, cross-equatorial Hadley cell expands into both the summer and winter hemispheres as  $\Omega$  decreases (e.g. Faulk et al. 2017; Singh 2019). But whereas in an Earth-like regime the summer  $\varphi_a$  and winter  $\varphi_d$  are comparably poleward, in slowly rotating cases the summer  $\varphi_a$  is farther poleward than the winter  $\varphi_d$ : the cross-equatorial Hadley cell becomes increasingly lopsided about the equator [e.g. Fig. 5 of Guendelman and Kaspi (2018), Fig. 12 of Guendelman and Kaspi (2019)].<sup>2</sup> Moreover, Guendelman and Kaspi (2019) empirically find distinct best-fit power-law exponents for the two edges, close to  $\varphi_a \propto \Omega^{-2/3}$  and  $\varphi_d \propto \Omega^{-1/2}$ . We will use our theory along with idealized GCM simulations to explain these exponents and how they relate to the lopsidedness of the cross-equatorial cell.

In the following sections we:

- derive and describe fixed-Ro zonal wind, angular momentum, and depth-averaged potential temperature fields (Section 2);
- present our unified theory, which essentially combines the KL12 model for  $\varphi_d$  with the Hill et al. (2021) theory for  $\varphi_a$  (Section 3);
- and test our theory against idealized GCM simulations, first over the annual cycle in one moist model and second for the solstitial Hadley circulation across rotation rates in one dry and two moist models (Section 4).

We then conclude with summary and discussion (Section 5).

## 2. Uniform-Ro fields

In general, absolute angular momentum is

$$M = a \cos \varphi (\Omega a \cos \varphi + u), \quad (1)$$

where  $a$  is planetary radius,  $\varphi$  is latitude, and  $u$  is the zonally averaged zonal wind. This can be considered the sum of planetary angular momentum,  $M_p(\varphi) \equiv \Omega a^2 \cos^2 \varphi$ , and relative angular momentum  $u a \cos \varphi$ . The corresponding AMC zonal wind field—for which angular momentum is meridionally uniform and equal to the planetary angular momentum value  $M_p(\varphi_a)$  at a specified latitude  $\varphi_a$ —is

$$u_{\text{amc}}(\varphi) = \Omega a \cos \varphi \left( \frac{\cos^2 \varphi_a}{\cos^2 \varphi} - 1 \right). \quad (2)$$

For the Hadley cells, we equate  $\varphi_a$  in (2) with the cells’ ascending edge on the grounds that ascent out of the viscous boundary layer there transmits the local planetary angular momentum,  $M_p(\varphi_a)$ , to the comparatively inviscid free troposphere (Held and Hou 1980; Lindzen and Hou 1988). This neglects the finite width of the ascent branch (Watt-Meyer and Frierson 2019; Byrne and Thomas 2019), but in principle one could compute an effective ascent latitude by averaging the planetary angular momentum over the full extent of the ascending branch, perhaps weighting by the vertical velocity out of the boundary layer at each latitude.

The Rossby number is defined as

$$\text{Ro} \equiv -\frac{\zeta}{f}, \quad (3)$$

where  $\zeta \equiv -(\cos \varphi)^{-1} \partial_\varphi (u \cos \varphi)$  is zonal-mean relative vorticity and  $f \equiv 2\Omega \sin \varphi$  is the planetary vorticity (i.e. the Coriolis parameter). Absolute vorticity is given by  $\eta = f + \zeta = f(1 - \text{Ro})$ . Absolute vorticity is proportional to the meridional gradient of angular momentum, and as such in an AMC state necessarily  $\eta = 0$  and  $\text{Ro} = 1$ . In discussing the GCM simulations below, we will make use of a generalized version of Ro (Singh 2019), but (3) is the quantity used in the fixed-Ro fields we now define.

From (3),  $\zeta = -\text{Ro} f$ . If  $\text{Ro} < 1$  but horizontally uniform, integrating meridionally yields the fixed-Ro zonal wind field,

$$u_{\text{Ro}}(\varphi) = \text{Ro} u_{\text{amc}}(\varphi), \quad (4)$$

which is simply the AMC zonal wind field scaled by Ro.<sup>3</sup> The corresponding angular momentum field is

$$M_{\text{Ro}}(\varphi) = \Omega a^2 [\text{Ro} \cos^2 \varphi_a + (1 - \text{Ro}) \cos^2 \varphi], \quad (5)$$

simplified, dry GCM. Zurita-Gotor and Held (2018) discuss the absolute vorticity distribution corresponding to uniform Ro.

<sup>2</sup>This strictly applies to non-axisymmetric atmospheres. It does not emerge clearly in simulations of axisymmetric atmospheres, which on theoretical grounds should exhibit  $\varphi_d$  poleward of  $-\varphi_a$  (Hill et al. 2019).

<sup>3</sup>Davis and Birner (2022) present what amounts to (4) (i.e.  $u_{\text{amc}}$  multiplied by a less-than-unity constant) from heuristic grounds albeit without reference to Ro; it should be noted that they also challenge the physical validity of baroclinic instability onset determining Hadley cell extent.

which is a Ro-weighted average of the planetary angular momentum at the ascent latitude,  $M_p(\varphi_a)$ , and the full meridional distribution of the planetary angular momentum,  $M_p(\varphi)$ .

Finally, though it does not enter into our model for the Hadley cell edges below, we present for a Boussinesq atmosphere (see e.g. Eq. 1 of Hill et al. (2019) for the full underlying system of equations) the depth-averaged potential temperature field in gradient balance with  $u_{Ro}$ . Denoted  $\hat{\theta}_{Ro}$ , it is given by

$$\frac{\hat{\theta}_a - \hat{\theta}_{Ro}(\varphi)}{\theta_0} = \frac{Ro}{2Bu} \left[ (2 - Ro) \cos^2 \varphi + \cos^2 \varphi_a \times \right. \quad (6)$$

$$\left. \left( 4(1 - Ro) \ln \left( \frac{\cos \varphi_a}{\cos \varphi} \right) + Ro \frac{\cos^2 \varphi_a}{\cos^2 \varphi} - 2 \right) \right],$$

where  $\hat{\theta}_a$  is the depth-averaged potential temperature at the latitude  $\varphi_a$ ,  $\theta_0$  is the Boussinesq reference potential temperature,

$$Bu \equiv \frac{gH}{(\Omega a)^2} \quad (7)$$

is the planetary Burger number with gravity  $g$  and tropopause height  $H$ , and we have assumed that  $u_{Ro}$  occurs near the tropopause while  $u \approx 0$  at the surface.

Fig. 1 shows example  $u_{Ro}$ ,  $M_{Ro}$ , and  $\hat{\theta}_{Ro}$  fields with  $Ro = 1, 0.5$ , or  $0.3$  and  $\varphi_a = 0^\circ$  or  $20^\circ$ . For zonal wind, irrespective of  $Ro$  and  $\varphi_a$ ,  $u_{Ro}$  vanishes at  $\varphi_a$  and increases monotonically moving away from the equator. If  $\varphi_a \neq 0$ ,  $u_{Ro}$  is negative from  $-\varphi_a$  to  $\varphi_a$ , minimizing at the equator. Both moving  $\varphi_a$  off equator and decreasing  $Ro$  act to make the westerlies less positive. For example, at  $30^\circ S/N$ ,  $u_{Ro} \approx 133, 67$ , and  $40 \text{ m s}^{-1}$  respectively for  $Ro = 1, 0.5$ , and  $0.3$  if  $\varphi_a = 0$  or  $71, 36$ , and  $21 \text{ m s}^{-1}$  respectively if  $\varphi_a = 20^\circ$ . For angular momentum, irrespective of  $Ro$  and  $\varphi_a$ ,  $M_{Ro}$  at  $\varphi_a$  is equal to the local planetary angular momentum  $M_p(\varphi_a)$ ; if  $Ro = 1$  all latitudes take this value. For  $Ro < 1$  it maximizes at the equator and decreases monotonically moving poleward. For the gradient-balanced potential temperature,  $\hat{\theta}_{Ro}$  maximizes at  $\varphi_a$  irrespective of  $Ro$  and  $\varphi_a$  and for  $\varphi_a \neq 0$  has a local minimum at the equator. As  $Ro$  increases, the meridional temperature gradients increase in magnitude, with a deeper equatorial dip and a more equatorward shoulder poleward of  $\varphi_a$  where temperatures begin dropping rapidly toward the pole.

### 3. Combined theory for Hadley cell ascending and descending edges

We now use these fixed-Ro fields to derive an expression for  $\varphi_d$  given values of  $Ro$  and  $\varphi_a$  that closely follows KL12. We then introduce within it our scaling for  $\varphi_a$ , yielding our unified theory for  $\varphi_d$  and  $\varphi_a$ . We then incorporate the influence of surface thermal inertia on the seasonal cycles of  $\varphi_a$  analytically and on  $\varphi_d$  more empirically.

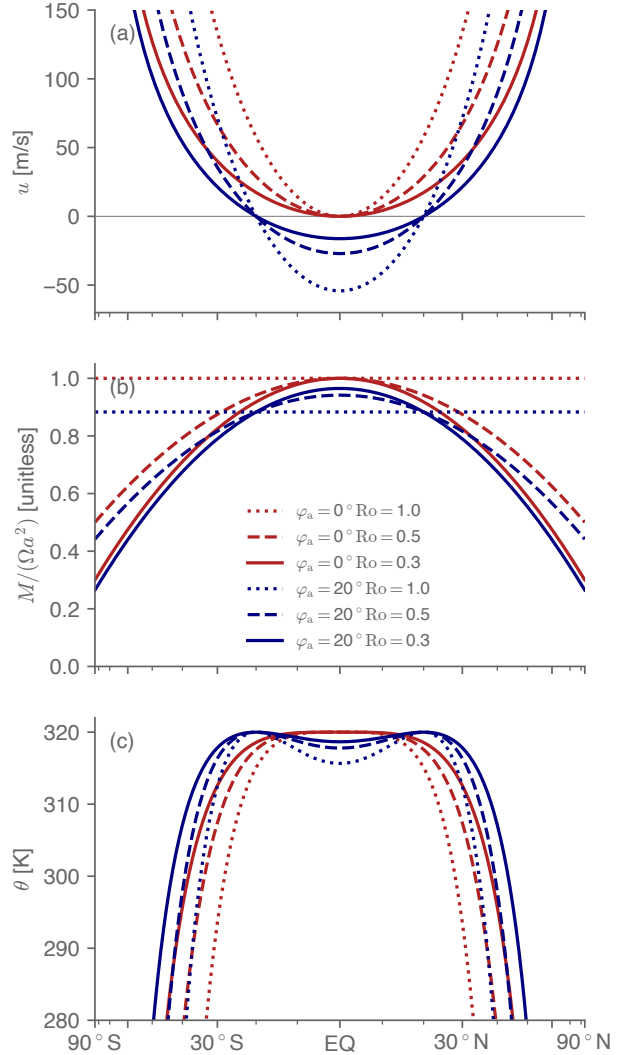


FIG. 1. Example (a) zonal wind ( $u_{Ro}$ , in  $\text{m/s}$ ), angular momentum ( $M_{Ro}$ , normalized by  $\Omega a^2$  and thus unitless), and depth-averaged potential temperature ( $\hat{\theta}_{Ro}$ , units Kelvin) fields under a uniform Rossby number. Red curves are for  $\varphi_a = 0$  and blue curves  $\varphi_a = 20^\circ S/N$ , while dotted, dashed, and solid curves are for  $Ro = 1.0, 0.5$ , and  $0.3$ , respectively. Horizontal axis spacing is in  $\sin \varphi$ .

#### a. Baroclinic instability onset theory for the Hadley cell edge with $Ro < 1$

Following H00, the baroclinic instability criterion for the two-layer model is approximately

$$\frac{u}{\Omega a} = Bu \Delta_v \frac{\cos \varphi}{\sin^2 \varphi}, \quad (8)$$

where  $u$  is the zonal wind in the upper layer, the wind in the lower layer has been assumed small enough to neglect, and  $\Delta_v$  is a static stability parameter representing the bulk frac-

tional increase in potential temperature from the surface to the tropopause.<sup>4,5</sup> H00 applies this to the annual-mean Hadley cells by assuming on-equatorial ascent, that the zonal winds are AMC, and that the descending edge is identical to this baroclinic instability onset latitude. Formally, taking  $\varphi_a \approx 0$ , using (2) for  $u$  in (8), and taking the small-angle limit yields the original H00 theory for  $\varphi_d$ , which we denote  $\varphi_{H00}$ :

$$\varphi_{H00} = (\text{Bu}\Delta_v/\text{Ro})^{1/4}. \quad (9)$$

Using  $u_{\text{Ro}}$  (4) rather than  $u_{\text{amc}}$  (2) as the zonal-wind profile in (8), for  $\text{Ro} < 1$  the predicted cell edge becomes

$$\varphi_{\text{Ro,ann}} = \left( \frac{\text{Bu}\Delta_v}{\text{Ro}} \right)^{1/4} = \text{Ro}^{-1/4} \varphi_{H00}, \quad (10)$$

with  $\varphi_{H00}$  given by (9). This displaces the cell edge prediction poleward by, for example,  $\sim 19\%$  if  $\text{Ro} = 0.5$  or  $\sim 50\%$  if  $\text{Ro} = 0.2$ . Using the original  $H = 10$  km and  $\Delta_v = 1/8$  parameter values from Held and Hou (1980) yields  $\text{Bu} \approx 0.46$  and  $\varphi_{H00} \approx 28^\circ$ , which becomes approximately  $33.3^\circ$  if  $\text{Ro} = 0.5$  or  $41.9^\circ$  if  $\text{Ro} = 0.2$ . This poleward displacement as  $\text{Ro}$  decreases coheres with physical intuition: because the upper-layer zonal wind magnitude at each latitude decreases as  $\text{Ro}$  decreases, the two-layer baroclinic instability onset criterion is met farther poleward.

For  $\varphi_a \neq 0$ , using (4) in (8) gives without approximation

$$\frac{\sin^4 \varphi_d}{\cos^2 \varphi_d} - \sin^2 \varphi_a \frac{\sin^2 \varphi_d}{\cos^2 \varphi_d} - \frac{\text{Bu}\Delta_v}{\text{Ro}} = 0, \quad (11)$$

where  $\varphi_d$  is the descending edge. From (10) the last term could equivalently be written  $-\varphi_{\text{Ro,ann}}^4$ . These arguments serve equally for the cross-equatorial, winter cell and the summer cell (provided it exists), depending on which cell the chosen  $\text{Ro}$  value is representative of. A corollary is that if the mean  $\text{Ro}$  value is the same in both cells, then the Hadley circulation extends equally far into either hemisphere irrespective of  $\varphi_a$ . Note that our assumption of uniform  $\text{Ro}$  throughout either cell differs slightly from KL12, who assume  $\text{Ro} = 1$  from the summer-hemisphere edge of the cross-equatorial cell to the equator, a uniform  $\text{Ro} \leq 1$  value in the winter hemisphere, and a uniform  $\text{Ro} \leq 1$  value throughout the summer cell.

We have performed a 2D parameter sweep over  $\varphi_a$  and  $(\text{Bu}\Delta_v/\text{Ro})^{1/4}$ , from  $0^\circ$  to  $90^\circ$  in  $1^\circ$  increments for  $\varphi_a$  and

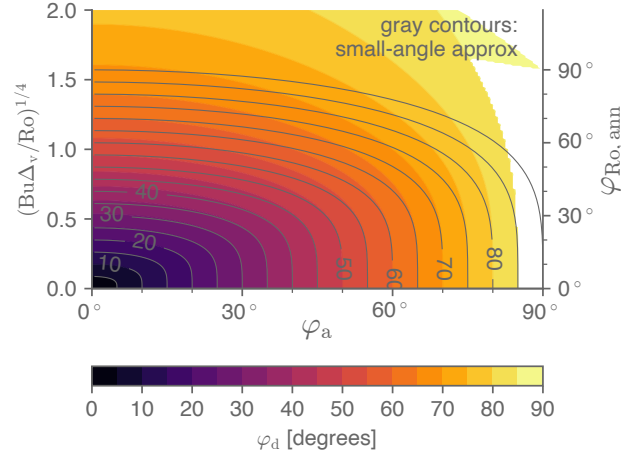


FIG. 2. Numerical solutions of (11) for values of  $\varphi_a$  and of  $(\text{Bu}\Delta_v/\text{Ro})^{1/4}$ , with  $\varphi_a$  sampled from  $0$  to  $90^\circ$  in  $1^\circ$  increments and  $(\text{Bu}\Delta_v/\text{Ro})^{1/4}$  (which is dimensionless) from  $0$  to  $2.0$  in  $0.01$  increments. The right vertical axis labels are the  $\varphi_{\text{Ro,ann}}$  solutions in degrees from  $0$  to  $90^\circ$  corresponding to the given  $(\text{Bu}\Delta_v/\text{Ro})^{1/4}$  values. Areas in white indicate that the simple numerical algorithm used did not converge, but clearly they correspond to  $\varphi_d$  very near the pole. Contours are from  $5$  to  $90^\circ$  in  $5^\circ$  increments according to the colorbar. Overlaid gray contours are the corresponding small-angle solutions obtained using (12), likewise from  $5$  to  $90^\circ$  in  $5^\circ$  increments.

from  $0$  to  $2$  in  $0.01$  increments for  $(\text{Bu}\Delta_v/\text{Ro})^{1/4}$ , solving (11) numerically for each pair of parameter values. The results are shown as shaded contours in Fig. 2.<sup>6</sup> Recalling that  $\varphi_{\text{Ro,ann}} \equiv (\text{Bu}\Delta_v/\text{Ro})^{1/4}$ , the right vertical axis shows the equivalent values of  $\varphi_{\text{Ro,ann}}$  up to  $90^\circ$ , above which the small-angle solution obviously is nonsensical but the full solution retains its validity. The value of  $\varphi_d$  increases monotonically with  $\varphi_a$  and with  $(\text{Bu}\Delta_v/\text{Ro})^{1/4}$ . Close to the vertical axis of Fig. 2,  $|\varphi_{\text{Ro,ann}}/\varphi_a| \gg 1$ , and  $\varphi_d \approx \varphi_{\text{Ro,ann}}$ :  $\varphi_a$  is negligibly off-equator. Close to the horizontal axis,  $|\varphi_{\text{Ro,ann}}/\varphi_a| \ll 1$ , and thus  $\varphi_d \approx \varphi_a$ . This regime usefully describes cases where the summer cell effectively disappears, as in all of the perpetual solstice simulations we will discuss below. For the winter hemisphere, the interpretation is that baroclinic instability onset occurs just poleward of  $-\varphi_a$ , near enough that it can be approximated as  $-\varphi_a$ . For intermediate values, if e.g.  $\varphi_a = \varphi_{\text{Ro,ann}}$ , then  $\varphi_d$  is displaced  $27\%$  poleward of  $\varphi_a$ . We note that  $|\varphi_d| \geq |\varphi_a|$ ; the descending edge latitude is always at or poleward of the ascending edge latitude. This is appropriate for the summer-hemisphere  $\varphi_d$  but will prove imperfect for the winter  $\varphi_d$  in the idealized GCM simulations across rotation rates discussed below.

<sup>4</sup>H00 uses the symbol  $R$  to denote the planetary Burger number, which elsewhere (Held and Hou 1980; Hill et al. 2019) is used for the thermal Rossby number. To prevent confusion we use the more explicit notation  $\text{Bu}$  for the planetary Burger number and  $\text{Ro}_{\text{th}}$  for the thermal Rossby number.

<sup>5</sup>The tropopause depth  $H$ , which for the H00 theory is strictly the local tropopause height, is assumed horizontally uniform and unmodified by the large-scale circulation from its forcing value corresponding to latitude-by-latitude radiative-convective equilibrium; see Hill et al. (2020) for justification.

<sup>6</sup>Over most of the parameter space this quartic equation has only two solutions, which correspond to  $\pm\varphi_d$ . Two additional solutions straddling very close to zero can appear for sufficiently large  $\varphi_a$  but are not physically meaningful.

Making the small-angle approximation for both  $\varphi_d$  and  $\varphi_a$  in (11) yields a closed expression for  $\varphi_d$ :

$$\varphi_d^2 = \varphi_a^2 \left( \frac{1}{2} + \sqrt{\frac{1}{4} + \frac{\text{Bu}\Delta_v}{\text{Ro}\varphi_a^4}} \right) = \varphi_a^2 \left( \frac{1}{2} + \sqrt{\frac{1}{4} + \left( \frac{\varphi_{\text{Ro,ann}}}{\varphi_a} \right)^4} \right), \quad (12)$$

This is shown as overlaid contours in Fig. 2. Only for  $(\text{Bu}\Delta_v/\text{Ro})^{1/4} \gtrsim 0.8$  does the small-angle approximation error exceed a few degrees latitude, irrespective of  $\varphi_a$ .

### b. Incorporating theory for $\varphi_a$

Using (12) requires knowledge of  $\varphi_a$ , which KL12 diagnose. Hill et al. (2021) derive a prognostic theory for  $\varphi_a$  as determined by the meridional extent of supercritical forcing, based on the following arguments. If no large-scale meridional overturning circulation existed, local radiative-convective equilibrium (RCE) must prevail at each latitude in the time mean. But given the resulting meridional temperature gradients driven by the meridional distribution of insolation, this hypothetical RCE state would generate zonal wind fields through gradient balance that are symmetrically unstable from the equator to some latitude in the summer hemisphere; the presence of this instability defines the tropical supercritical forcing extent (Plumb and Hou 1992; Emanuel 1995). A large-scale meridional overturning circulation therefore must emerge spanning at least the supercritical latitudes, and in axisymmetric atmospheres that circulation must be the Hadley cells. In eddying atmospheres, in principle the circulation that emerges over the supercritical region could be predominantly macroturbulent as in the extratropics rather than Hadley-like, but in practice the opposite occurs: the ascending edge latitude is poleward of—and, crucially, proportional to—the supercritical extent.

Formally, in the small-angle limit Hill et al. (2021) show that

$$\varphi_a = c_a \left( \frac{\text{Ro}_{\text{th}}}{2} \right)^{1/3}, \quad (13)$$

where  $(\text{Ro}_{\text{th}}/2)^{1/3}$  is the theoretical solution for the supercritical extent and  $c_a$  is the empirically determined proportionality constant.  $\text{Ro}_{\text{th}}$  is the thermal Rossby number,

$$\text{Ro}_{\text{th}} \equiv \text{Bu}\Delta_h \sin \varphi_m, \quad (14)$$

with  $\Delta_h$  the parameter of the imposed forcing (i.e. the latitude-by-latitude RCE state) that—in conjunction with  $\varphi_m$ , the latitude at which the forcing maximizes—determines the bulk meridional temperature gradients of the forcing. The same  $\text{Ro}_{\text{th}}^{1/3}$  scaling emerges in the semi-empirical, axisymmetric theory of Caballero et al. (2008), as well as (for sufficiently small  $\text{Ro}_{\text{th}}$ ) in numerical solutions of the original Lindzen and Hou (1988) axisymmetric, equal-area model of the solstitial Hadley cells (Guen-

delman and Kaspi 2018). The Hill et al. (2021) scaling (13) emerges from a less strict set of assumptions than Caballero et al. (2008) and presupposes neither axisymmetry nor anything about the resulting circulation's zonal wind and energy transport fields, unlike the equal-area model. Moreover, the solstitial equal-area model (Lindzen and Hou 1988) predicts implausibly large Hadley cells for Earth as  $\varphi_m$  moves more than a few degrees off equator (Hill et al. 2019) and is biased poleward against numerical simulations in an idealized GCM over a wide range of planetary parameter values (c.f. Fig. 15a of Guendelman and Kaspi 2019).

For the solstitial, cross-equatorial Hadley cells in the simulations analyzed by Hill et al. (2021) the best-fit value of  $c_a$  ranges from 1.3 to 2.6 across three idealized GCMs.<sup>7</sup> For  $\text{Ro}_{\text{th}}$ , Hill et al. (2021) show that for solstitial seasons one can attain an accurate estimate with  $\varphi_m$  set to  $90^\circ$  by tuning the value of  $\Delta_h$ . Doing so, the non-standard  $\sin \varphi_m$  term drops out and the  $\text{Ro}_{\text{th}}$  definition becomes the more conventional  $\text{Ro}_{\text{th}} = \text{Bu}\Delta_h$ . But the  $\sin \varphi_m$  dependence is necessary for understanding the annual cycle as will be discussed further below (see also Fig. 15 of Guendelman and Kaspi 2020).

Given diagnosed values of  $c_a$  and  $\text{Ro}$  for each Hadley cell, (13) in conjunction with (12) provide a theory for all three cell edges: (13) predicts  $\varphi_a$ , and using that in (12) for  $\varphi_d$  then yields

$$\varphi_d = c_d c_a \left( \frac{\text{Ro}_{\text{th}}}{2} \right)^{1/3} \sqrt{\frac{1}{2} + \sqrt{\frac{1}{4} + \frac{2^{4/3}}{c_a^4} \frac{\Delta_v}{\Delta_h \sin \varphi_m} \frac{1}{\text{Ro}\text{Ro}_{\text{th}}^{1/3}}}}, \quad (15)$$

where we have also included the empirical fitting parameter  $c_d$  that will prove necessary for the simulations analyzed below. The term  $\Delta_v/\Delta_h \sin \varphi_m$ , which is the ratio of the planetary-scale vertical to horizontal fractional potential temperature changes of the latitude-by-latitude RCE state, amounts to a seasonally varying bulk isentropic slope of the forcing. From (15), the poleward edge of either Hadley cell increases with increasing  $\text{Ro}_{\text{th}}$ , increasing RCE isentropic slope, or decreasing  $\text{Ro}$ . Large  $\text{Ro}_{\text{th}}$  corresponds to the large- $\varphi_a$  limit above,  $\varphi_d \approx \varphi_a$ , while small  $\text{Ro}_{\text{th}}$  corresponds to the small- $\varphi_a$  limit of  $\varphi_d \approx \varphi_{\text{Ro,ann}}$ .

### c. Influence of surface thermal inertia on the $\varphi_a$ seasonal cycle

Because insolation varies seasonally, any nonzero thermal inertia of the surface mixed layer damps and delays the surface thermal response, the more so the larger the mixed layer heat capacity. This is true of the dynamically equilibrated climate but also the hypothetical latitude-by-latitude

<sup>7</sup>Hill et al. (2021) report values for  $c_a$  of 1.0, 1.7, and 2.1 for the Faulk et al. (2017), Singh (2019), and (Hill et al. 2021) simulations, respectively, but these implicitly incorporate the  $2^{-1/3} \approx 0.8$  factor in (13). We separate it out from  $c_a$  for better consistency with (13).

RCE state that determines  $\varphi_a$ . We therefore now define an “effective” thermal forcing based on the analytical model of Mitchell et al. (2014) which leaves the functional form of (13) for  $\varphi_a$  intact but modifies the  $\varphi_m$  term within  $\text{Ro}_{\text{th}}$  to be damped and delayed in its seasonal excursions. We refer the interested reader to Mitchell et al. (2014) for details, presenting here only the end results of how  $\varphi_m$  is modified.

First consider the unmodified  $\varphi_m$  annual cycle. For Earth’s present-day insolation, during equinoctial seasons there is only one maximum in  $\varphi_m$ , but during solstitial seasons there are two maxima in the summer hemisphere, a local one near  $44^\circ$  and the global maximum at the summer pole (see e.g. Fig. 1 of Hill et al. 2021). Though the polar maximum is relevant for the global-scale Hadley cells in other planetary atmospheres (Singh 2019), for Earth we can comfortably consider the mid-latitude maximum at solstice to be  $\varphi_m$ . An advantage of this choice is that, combining the equinoctial and solstitial seasons, this yields a nearly sinusoidal annual cycle of  $\varphi_m$  (not shown):  $\varphi_m \approx \varphi_{m,\text{ann}} \cos(\omega_{\text{orb}}(t - t_{\text{solst}}))$ , where  $\varphi_{m,\text{ann}} = 44^\circ$  is the annual maximum value of  $\varphi_m$ ,  $\omega_{\text{orb}}$  is the orbital frequency,  $t$  is the time of year, and  $t_{\text{solst}}$  is the time of year of northern summer solstice.

Next, c.f. Mitchell et al. (2014) we define the ratio of the seasonal timescale to the thermal inertial timescale as  $\alpha \equiv (\omega_{\text{orb}}\tau_{\text{ti}})^{-1}$ , where  $\tau_{\text{ti}} = C_{\text{ml}}/4\sigma\bar{T}^3$  is the thermal inertia timescale with  $C_{\text{ml}}$  the surface mixed-layer heat capacity,  $\sigma$  the Stefan-Boltzmann constant, and  $\bar{T}$  the annual-mean, global-mean temperature. The heat capacity of the mixed layer is given by  $C_{\text{ml}} = \rho_w c_w H_{\text{ml}}$ , where  $\rho_w$  is the density of liquid water,  $c_w$  is the heat capacity of liquid water, and  $H_{\text{ml}}$  is the depth of the mixed layer. Using values of  $\rho_w = 1000 \text{ kg m}^{-3}$ ,  $c_w = 4186 \text{ J kg}^{-1} \text{ K}^{-1}$ , and taking  $H_{\text{ml}} = 10 \text{ m}$  as used in the simulation to be discussed, we have  $C_{\text{ml}} \approx 4.186 \times 10^7 \text{ J m}^{-2} \text{ K}^{-1}$ . Then using  $\bar{T} = 288 \text{ K}$  and  $\sigma = 5.67 \times 10^{-8} \text{ W m}^{-2} \text{ K}^{-4}$ , the thermal inertia timescale is  $\tau_{\text{ti}} \approx 89$  days. Using  $\omega_{\text{orb}} = 2\pi/365 \text{ days}^{-1}$  we have  $\alpha \approx 0.65$ , an intermediate value: the thermal inertial and seasonal cycle timescales are comparable, meaning that the effective  $\varphi_m$  annual cycle will be moderately damped and phase-lagged from the insolation. C.f. Appendix A of Lee and Mitchell (2021), this yields a damping factor to  $\varphi_m$  of  $\alpha/\sqrt{1+\alpha^2} \approx 0.55$  and a lag of  $\tau_{\text{lag}} = \omega_{\text{orb}}^{-1} \arcsin(\alpha/\sqrt{1+\alpha^2}) \approx 33$  days: roughly, the effective  $\varphi_m$  is damped by half and delayed by one month. These values will prove fairly accurate in predicting  $\varphi_a$  in the simulation discussed next, albeit with an additional ~two-week lag added empirically for a best fit.

For the timescale of  $\varphi_d$  relative to the seasonal cycle, we proceed much more empirically. Insofar as  $\varphi_d$  is determined by the combination of  $\varphi_a$  and  $\text{Ro}$  as we have posited, one relevant timescale is that of the upper-level zonal wind adjustment: it takes a finite amount of time for the zonal winds in the descending branch to adjust to a change in  $\varphi_a$  in the opposite hemisphere. The other is the timescale

of changes in  $\text{Ro}$ , however we lack clear intuition for what controls  $\text{Ro}$  and thus this timescale (see the Discussion below for some speculation); moreover a time-invariant  $\text{Ro}$  seems to fit the simulation well as shown below. We find empirically that the best fit to the simulated  $\varphi_d$  occurs by lagging our predicted  $\varphi_d$  based on the contemporaneous  $\text{Ro}$  and  $\varphi_a$  by roughly one month, which seems not radically too long nor short.

#### 4. Simulation results

We now assess these theoretical arguments against simulations in three idealized GCMs. After describing the models and simulations, we consider the annual cycles of  $\varphi_d$  and  $\varphi_a$  in an Earth-like aquaplanet control simulation, followed by their behaviors across a wide range of rotation rates in all three GCMs.

##### a. Description of models and simulations

Details of the model formulations and simulations are provided by Hill et al. (2021). Briefly, the dry model (Schneider 2004) approximates radiative transfer via Newtonian cooling, with the equilibrium temperature field that temperatures are relaxed toward being the forcing field from Lindzen and Hou (1988) but maximizing at the north pole (i.e. setting  $\varphi_m = 90^\circ$ ). The relaxation field is statically unstable, and a simple convective adjustment scheme relaxes over a fixed timescale the temperatures of unstable columns toward a lapse rate of  $\gamma\Gamma_d$ , where  $\Gamma_d = g/c_p$  is the dry adiabatic lapse rate with  $c_p$  the specific heat of dry air at constant pressure, and  $\gamma = 0.7$  mimics the stabilizing effects of latent heat release that would occur in a moist atmosphere (though the model is otherwise dry). Four simulations are performed, three with the  $\Delta_h$  parameter that determines the horizontal temperature gradients of the forcing set to 1/15 and with the planetary rotation rate set to 0.25, 1, or  $2\times$  Earth’s value, and another with  $\Delta_h = 1/6$  and Earth’s rotation rate. The  $\Delta_h = 1/6$  value is conventional (Lindzen and Hou 1988), but Hill et al. (2021) show that, for  $\varphi_m = 90^\circ$ ,  $\Delta_h \approx 1/15$  is the best fit to numerically simulated latitude-by-latitude RCE.

The moist simulations are those originally presented by Faulk et al. (2017) and Singh (2019). The Faulk et al. (2017) simulations use the idealized aquaplanet model of Frierson et al. (2006) featuring a slab-ocean lower boundary with a 10-m mixed layer depth. They are forced either with an annual cycle of insolation approximating that of present-day Earth or with insolation fixed at northern summer solstice. The annual cycle simulations include planetary rotation rates ranging from 1/32 to  $4\times$  Earth’s by factors of two, while the three perpetual solstice simulations are at 1, 1/8, or  $1/32\times$  Earth’s rotation rate. The Singh (2019) simulations use an idealized aquaplanet close to that of O’Gorman and Schneider (2008), itself a modified version of the Frierson et al. (2006) model. All of



these simulations use a time-invariant, solstitial insolation forcing as in the second subset of the Faulk et al. (2017) simulations, with rotation rates ranging from  $1/8$  to  $8\times$  Earth's.

The simulated values of  $\varphi_d$  are diagnosed conventionally as the latitude at which the mass-overturning streamfunction at the level of the cell center reaches 10% of its maximum value, with an additional  $\cos \varphi$  weighting factor that accounts for constricting latitude circles moving poleward (Singh 2019). The 10% threshold is needed rather than a zero crossing for cases with large Hadley cells, in which the Ferrel cells and/or summer Hadley cell can be nonexistent and the streamfunction same-signed (albeit very weak) all the way to either pole. For  $\varphi_a$ , the same 10% threshold is used in the perpetual-solstice simulations and in the annual cycle simulations for months in which the summer Hadley cell has effectively vanished. In months where both Hadley cells are well defined,  $\varphi_a$  is taken as the average of the inner edges of the two cells computed using this 10% criterion (which is approximately the latitude of the streamfunction zero crossing; not shown).

#### b. Annual cycles of $\varphi_a$ and $\varphi_d$

Before presenting the simulation results, we delineate three regimes regarding the relative importance of  $Ro$  vs.  $\varphi_a$  in determining  $\varphi_d$ . First is where  $Ro$  predominates: by (12) if  $\varphi_a$  is small relative to  $\varphi_{Ro,ann} = (Bu\Delta_v/Ro)^{1/4}$  throughout the annual cycle, then the annual cycle of  $\varphi_d$  is determined by the annual cycle of  $Ro$  (provided that  $\Delta_v$  and  $H$  are constant across seasons). Second is intermediate, with both  $Ro$  and  $\varphi_a$  influential as in the compensation regarding the winter  $\varphi_d$  found by KL12 in CMIP3 simulations:  $\varphi_a$  is farthest poleward at solstice, acting to move  $\varphi_d$  poleward, but  $Ro$  is largest in the solstitial cross-equatorial cell, acting to move the winter  $\varphi_d$  equatorward. Third is where  $\varphi_a$  predominates, as we now show holds for the seasonally forced simulation at Earth's rotation rate of Faulk et al. (2017):  $\varphi_a$  variations (which are well predicted by supercriticality provided thermal inertia is accounted for) with  $Ro = 1$  assumed throughout the annual cycle account for the annual cycle of the winter  $\varphi_d$ .

Fig. 3 shows the climatological annual cycles of  $\varphi_a$  (solid red curve), of  $\varphi_d$  in both hemispheres (solid blue curves), and of the meridional overturning streamfunction at 500 hPa (color shading), as well as theoretical estimates described below for each cell edge. The simulated cells are Earth-like in their total meridional extent ( $\varphi_d$  varies over  $21.3$ – $27.7^\circ$ N and  $21.7$ – $26.5^\circ$ S) and annual cycle phasing, with  $\varphi_a$  migrating into either summer hemisphere with a  $\sim 1$ -month lag behind the insolation. However, the  $\varphi_a$  excursions are excessive,  $25.7^\circ$ S– $23.2^\circ$ N, resulting in an excessively rapid transition from equinoctial to solstitial regimes, approaching closer to the square-wave prediction of Lindzen and Hou (1988) for axisymmetric atmospheres

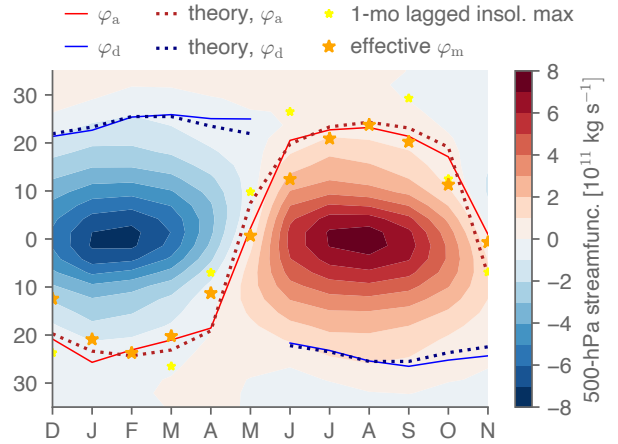


FIG. 3. In the seasonally forced, Earth-like aquaplanet simulation, climatological annual cycle of Hadley cell streamfunction at 500 hPa in shading according to the colorbar, as well as Hadley cell edges and theories for the Hadley cell edges as indicated in the legend. The effective  $\varphi_m$  is the effective insolation maximum for that month given the damping and delaying effects of thermal inertia on the seasonally varying forcing. The insolation maximum (yellow stars) is lagged by one month from its actual value to facilitate comparison with  $\varphi_a$ , and in the two months nearest solstice the maximum is near the summer pole and thus not shown.

than Earth's more sinusoidal variations (Dima and Wallace 2003).<sup>8</sup> This results in the summer cell being too weak, such that  $\varphi_d$  is only well defined in the winter half-year for either hemisphere (December through May for the northern hemisphere, June through November for the southern hemisphere). These discrepancies seem attributable to the rather shallow 10-m surface mixed layer, which promotes excessive seasonality (Donohoe et al. 2014; Wei and Bordoni 2018). Nevertheless the variations in  $\varphi_d$  and  $\varphi_a$ —in particular that the  $\varphi_d$  ranges are comparable to Earth's and several times smaller than that of  $\varphi_a$ —lead us to consider this useful enough for Earth.

The insolation maximum is near the summer pole during the core solstitial months and within the tropics otherwise (yellow stars, lagged by 1 month to ease comparison with  $\varphi_a$ ). The effective  $\varphi_m$  accounting for thermal inertia as described above.  $\varphi_a$  stays within the tropics always, with  $\varphi_a \approx \varphi_m$  to a reasonable degree. The supercriticality scaling (13) yields an even better prediction (dotted dark red curve), calculated as follows. Hill et al. (2021) perform a 2D parameter sweep of  $\varphi_m$  and  $\Delta_h$  to determine best fits of the Lindzen and Hou (1988) thermal forcing profile against numerical simulations of latitude-by-latitude RCE under solstitial forcing; for  $\varphi_m \approx 44^\circ$  the best fit over the Tropics occurs for  $\Delta_h = 1/8$  (approximately twice that of

<sup>8</sup>In fact the annual-mean rainfall and Hadley cells both show a double ITCZ resulting from this rapid jumping of the ascent fairly deep into either summer hemisphere (not shown).

the  $\Delta_h \approx 1/15$  value for  $\varphi_m = 90^\circ$ .<sup>9</sup> We therefore take  $\Delta_h = 1/8$ . With  $\Delta_h$  set, the proportionality constant  $c_a$  is left effectively as a fitting parameter, which by eye provides the best fit for  $c_a \approx 1.9$ .<sup>10</sup> The prediction is clearly not without empiricism, but nevertheless we are pleased with the overall accuracy against the simulated  $\varphi_a$ .

We then use this theoretically computed  $\varphi_a$  as just described to predict  $\varphi_d$ . Due to an inadvertent loss of zonal-wind data from the Faulk et al. (2017) simulations, we are not able to directly diagnose Ro. Instead, we assume  $\text{Ro} = 1$ , which provided  $0 \leq \text{Ro} \leq 1$  yields the equatorward-most possible  $\varphi_d$  predictions, all else equal. Even still, this yields a  $\varphi_d$  prediction poleward of the simulated  $\varphi_d$  values (not shown), which we correct for by setting  $c_d = 0.75$  in (15). We then shift the results later in time by one month, resulting in a fairly accurate fit to the simulations (dotted blue curve). In the concluding section below we provide speculative arguments to justify this equatorward displacement and 1-month phase lag of  $\varphi_d$  compared to  $\varphi_a$  (which in turn lags the insolation by  $\sim 1.5$  months). The  $\varphi_d$  prediction is only marginally improved if the actual simulated  $\varphi_a$  values are used rather than our predicted  $\varphi_a$  (not shown).

Because the monthly variations of  $\varphi_d$  are comparable to those of the comprehensive GCMs shown by KL12 ( $\lesssim 5^\circ$  about their annual means), we infer that muted annual cycles of  $\varphi_d$  relative to that of  $\varphi_a$  can emerge via different mechanisms even restricting to Earth-like conditions. On the one hand are the comprehensive GCMs analyzed by KL12: the seasonal Ro values (that KL12 indirectly diagnose as a fitting parameter) span 0.45–1, and  $\varphi_a$  presumably varies closer to the real-world value and thus less than in our aquaplanet simulations. On the other hand is our aquaplanet simulation:  $\varphi_d$  variations (provided  $c_d$  and the 1-month lag from  $\varphi_a$  are accounted for) appear determined almost entirely by the seasonality of  $\varphi_a$  with Ro treated as constant.

The theoretical predictions are also relatively insensitive to a reasonable range of parameter values. By (12), using conventional values of  $H = 10$  km and  $\Delta_v = 1/8$ , then for Earth  $\text{Bu} \approx 0.46$  and  $\text{Bu}\Delta_v \approx 0.06$ . Then varying  $\varphi_a$  over  $0$ – $15^\circ$ , and Ro over the KL12-reported Ro range of 0.45–1 yields a  $\varphi_d$  range of  $28.0$  to  $35.9^\circ$  (for  $\varphi_a = 0$ ,  $\text{Ro} = 1$  and  $\varphi_a = 15^\circ$ ,  $\text{Ro} = 0.45$  respectively). Moreover, the  $\varphi_d$

range is fairly insensitive to Ro if  $\varphi_a$  is held fixed and likewise to  $\varphi_a$  if Ro is held fixed: if Ro is fixed at unity, the  $\varphi_a = 15^\circ$  prediction moves equatorward only by  $1.7^\circ$ , and conversely if  $\varphi_a$  is at the equator the  $\text{Ro} = 0.45$  prediction moves poleward by only  $2.1^\circ$ .

### c. Relative behaviors of solstitial $\varphi_a$ and $\varphi_d$ across rotation rates

From (13),  $\varphi_a \propto \text{Ro}_{\text{th}}^{1/3}$ , which Hill et al. (2021) show accurately describes the solstitial  $\varphi_a$  across planetary rotation rates in the simulations presently under consideration. For  $\varphi_d$ , by (11) for small  $\text{Ro}_{\text{th}}$  and thus small  $\varphi_a$ ,

$$\varphi_d \approx c_d \left( \frac{\text{Bu}\Delta_v}{\text{Ro}} \right)^{1/4} = c_d \left( \frac{\text{Ro}_{\text{th}} \Delta_v}{\text{Ro} \Delta_h} \right)^{1/4}, \quad (16)$$

again incorporating the empirical fitting parameter  $c_d$ . In that case, provided Ro does not change appreciably then  $\varphi_d \propto \text{Bu}^{1/4} \sim \text{Ro}_{\text{th}}^{1/4}$ , where in this context we can substitute  $\text{Ro}_{\text{th}}$  for Bu since only  $\Omega$  is varied and appears identically (as  $\Omega^{-2}$ ) in the two nondimensional numbers. We now argue that the idealized GCM simulations reflect this modest  $1/3 - 1/4 = 1/12$  difference in power-law exponent in  $\text{Ro}_{\text{th}}$  for  $\varphi_a$  vs.  $\varphi_d$ .

Fig. 4(a) shows the winter  $\varphi_d$  for all the simulations as a function of  $\text{Ro}_{\text{th}}^{1/4}$ . For each model, a best-fit line is included of  $\varphi_d$  with  $\text{Ro}_{\text{th}}^{1/4}$ , restricting to simulations in the linear regime of  $\varphi_d$  vs.  $\text{Ro}_{\text{th}}^{1/4}$ .<sup>11</sup> Overall the simulations follow this scaling well. Table 1 lists the slope and intercept from the linear best fits of  $\varphi_d$  against  $\text{Ro}_{\text{th}}^{1/4}$ , with the slope amounting to a best fit for the empirical  $c_d$  parameter in (15) (at least in the small- $\text{Ro}_{\text{th}}$  limit). The inferred  $c_d$  values range from 1.4 for the Singh (2019) simulations to 0.9 for the Faulk et al. (2017) perpetual solstice simulations. The value of 1.0 for the Faulk et al. (2017) seasonal cycle simulations is modestly higher than the value discussed above of 0.8 for the climatological annual cycle in the Faulk et al. (2017) simulation at Earth’s rotation rate—opposite to  $c_a$ , which was larger for the annual cycle than across rotation rates. The intercepts, which in theory should be zero, range from  $-2.4$  to  $5.6^\circ$  latitude and average across the simulation sets to a modest  $0.3^\circ$ .

Table 1 includes best-fit power law exponents for  $\varphi_d$  and for  $\varphi_a$  against  $\text{Ro}_{\text{th}}$  computed for each set of simulations by linear regression in log-log space. For all sets of simulations, the inferred exponent is larger and closer to  $1/3$  for  $\varphi_a$  than for  $\varphi_d$ , which is closer to  $1/4$ . The dry simulations exhibit the largest exponents for both, 0.41 and 0.3, respectively, and the Faulk et al. (2017) seasonally forced and perpetual-solstice simulations, respectively, give the

<sup>9</sup>For the annual-mean rather than solstitial RCE state, Hill et al. (2020) diagnose a similar  $\Delta_h \approx 1/8$  value based on numerical RCE simulations under annual-mean insolation. This value is considerably larger than the solstitial one, which suggests that  $\Delta_h$  would be even larger under equinoctial forcing. But we do not attempt to account for this seasonality in  $\Delta_h$ .

<sup>10</sup>This value of  $c_a$  is  $\sim 45\%$  larger than the best-fit value of 1.31 (Hill et al. 2021) for the solstitial  $\varphi_a$  across the Faulk et al. (2017) seasonally forced simulations with different rotation rates—a neither trivial nor order-of-magnitude difference, suggesting that the proportionality is moderately influenced by different processes in these two distinct contexts. The 1.9 value is also less than the values of 2.2 and 2.6 diagnosed across rotation rates for, respectively, the simulations of Singh (2019) and the dry simulations of Hill et al. (2021).

<sup>11</sup>The extents of this linear regime (as well as the individual  $\varphi_a$  and  $\varphi_d$  values) differ appreciably between the two moist models, which are very similarly formulated, for reasons we do not understand. It spans  $\text{Ro}_{\text{th}} \lesssim 1$  for the Singh (2019) simulations vs.  $\text{Ro}_{\text{th}} \lesssim 1.5$  for the Faulk et al. (2017) simulations.



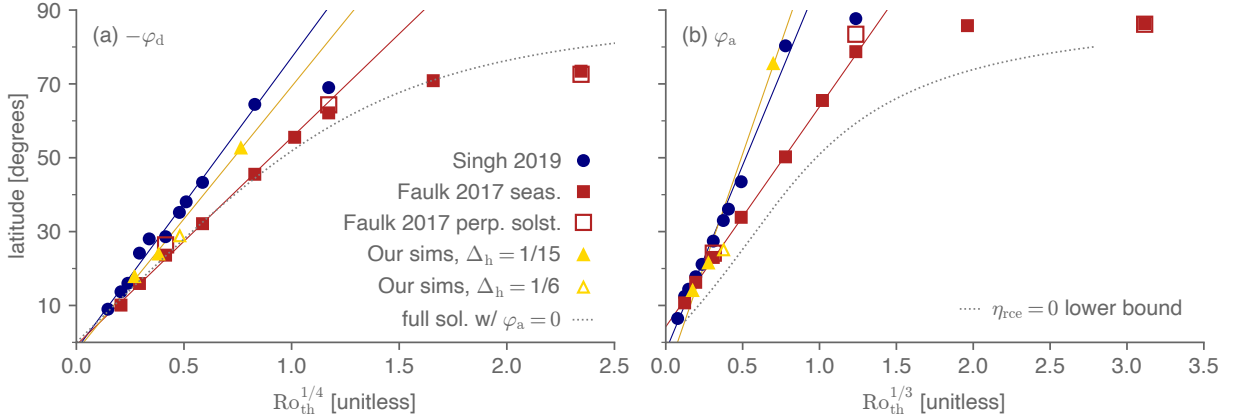


FIG. 4. In panel (a), latitude of the winter-hemisphere descending edge of the cross-equatorial Hadley cell,  $\varphi_d$ , in idealized aquaplanet simulations of Faulk et al. (2017), Singh (2019), and in the idealized dry simulations of Hill et al. (2021) as a function of the thermal Rossby number to the one-fourth power, each signified by different symbols as indicated in the legend. The solid lines show the linear best fit for  $\varphi_d$  as a function of  $\text{Ro}_{\text{th}}^{1/4}$  for the given simulation set, restricting to  $\text{Ro}_{\text{th}} < 1$ , with red, blue, and yellow for the Singh (2019), Faulk et al. (2017), and the  $\Delta_h = 1/15$  dry simulations respectively. The dotted grey curve is the numerical solution to (11) with  $\varphi_a = 0$  and  $\text{Ro}\Delta_h/\Delta_v = 1$ . Panel (b), which replicates Fig. 6 of Hill et al. (2021), are the corresponding quantities for the summer, ascending edge  $\varphi_a$ , with the horizontal axis spacing being  $\text{Ro}_{\text{th}}^{1/3}$ , and the dashed grey curve being the numerical solution to the full expression for the extent of supercritical forcing.

smallest exponents, 0.28 and 0.21. The average of the best-fit exponents across the four simulation sets are nearly identical to the scalings, 0.26 and 0.33.

As  $\text{Ro}_{\text{th}}$  increases beyond  $\sim 1$ , the simulated  $\varphi_d$  level off, never exceeding  $\sim 70^\circ$ . The full, non-small-angle expression (11) solved numerically with  $\varphi_a = 0$  and all parameters except  $\Omega$  set to Earth-like values (dotted grey curve) qualitatively captures this. This contrasts with  $\varphi_a$ —shown in Fig. 4(b) as a function of  $\text{Ro}_{\text{th}}^{1/3}$  (reproducing Fig. 6 of Hill et al. 2021)—which in the slowly-rotating regime is near the summer pole (Hill et al. 2021). In other words, as rotation rate decreases the cross-equatorial Hadley cell becomes increasingly lopsided, in the slowly rotating regime extending effectively to the summer pole but not the winter pole. As noted above, the solutions (11) and (12) for  $\varphi_d$  always predict  $|\varphi_d| \geq |\varphi_a|$ , and as such to explain the  $|\varphi_d| < |\varphi_a|$  cases we must appeal to the empirical proportionality constants  $c_a$  and  $c_d$  introduced in (13) and (15) as follows.

If  $\text{Ro}$  and the forcing isentropic slope  $\Delta_v/\Delta_h$  are both approximately unity, it can be shown from (13) and (16) that  $\varphi_a = \varphi_d$  provided that  $2^{1/3}c_d/c_a = \text{Ro}_{\text{th}}^{1/12}$ . Table 1 includes the slope and intercepts of  $\varphi_a$  against  $\text{Ro}_{\text{th}}^{1/3}$ , with the slope amounting to a best fit for  $c_a/2^{1/3}$  in (13). From Table 1 then, the ratio  $2^{1/3}c_d/c_a$  takes values approximately over 0.6-1 in the four simulation sets. Given the 0.6-1 range for the left-hand-side, this yields  $\text{Ro}_{\text{th}} \approx 1$ , with  $\varphi_d$  equatorward of  $\varphi_a$  for larger  $\text{Ro}_{\text{th}}$ . This roughly captures the behavior of the simulations. Of course, the slowly rotating regime with  $|\varphi_a| > |\varphi_d|$  extends beyond the regime where the small-angle power-law scalings being appealed

to are credible, but it nevertheless begins within the small-angle regime.

The unfilled yellow triangle in Fig. 4 shows the dry, LH88-forced simulation at Earth’s rotation rate with  $\Delta_h = 1/6$  rather than  $\Delta_h = 1/15$  as in the other three dry simulations. As is the case for  $\varphi_a$  (Hill et al. 2021),  $\varphi_d$  is somewhat separated from the power law of the  $\Delta_h = 1/15$  cases. Strictly speaking, in the  $\varphi_a \approx 0$  limit of (11),  $\varphi_d$  is independent of  $\Delta_h$ . But, while small,  $\varphi_a \neq 0$  in the simulations, and since an increase in  $\Delta_h$  moves  $\varphi_a$  poleward, it is qualitatively consistent that  $\varphi_d$  moves poleward as a result. Given that the annual cycle amounts to a variation in  $\Delta_h \sin \varphi_m$ , it is worth noting that the slope between the  $\Delta_h = 1/15$  and  $\Delta_h = 1/6$  cases at Earth’s rotation rate is shallower than that inferred across rotation rates at  $\Delta_h = 1/15$ , which qualitatively coheres with  $c_d$  being smaller for the annual cycle than across rotation rates in the Faulk et al. (2017) simulations (Table 1). A caveat, however, is that the deviation of the  $\Delta_h = 1/6$  case is modest; whether  $\Delta_h = 1/6$  cases at different rotation rates or other  $\Delta_h$  values would actually yield a different slope remains an open question.

#### d. Validity of the uniform-Ro assumption

Finally, we assess the validity of treating the upper-tropospheric  $\text{Ro}$  as uniform within each Hadley cell. Fig. 5 shows the meridional profile of  $\text{Ro}$  at 300 hPa in each simulation of Singh (2019), computed both conventionally as (3) and, following Singh (2019), in a generalized form

	winter $\varphi_d$			summer $\varphi_a$		
	power	$c_d$	intercept	power	$c_a/2^{1/3}$	intercept
theory	0.25	n/a	0°	0.33	n/a	0°
S19	0.28	1.4	-1.9°	0.34	1.8	-2.3°
F17, seas. forc.	0.26	0.9	0.2°	0.28	1.1	4.0°
F17, perp. solst.	0.21	0.9	5.7°	0.30	1.1	4.4°
dry, LH88-forced	0.26	1.3	-2.4°	0.41	2.1	-9.2°
F17, ann. cyc.	n/a	0.8	n/a	n/a	1.9	n/a

TABLE 1. Best-fit exponents of power law scalings for the winter and summer edges of the cross-equatorial solstitial Hadley cell in each set of simulations, as well as the best-fit slope and intercepts for each simulation set against the theoretical  $\text{Ro}_{\text{th}}$  power law. The slope for  $\varphi_d$  amounts to an approximation of  $c_d$  and that of  $\varphi_a$  an approximation of  $c_a$ ; the latter is reported with the additional  $2^{-1/3}$  factor included to facilitate direct comparison with  $c_d$ . Simulations are restricted to those for which  $\text{Ro}_{\text{th}} < 2$ , since the theoretical predictions of 1/3 and 1/4 for the winter and summer edges, respectively, assume small angle and thus small  $\text{Ro}_{\text{th}}$ . The dry LH88-forced simulations do not include the  $\Delta_h = 1/6$  case. S19 stands for Singh (2019), and F17 stands for Faulk et al. (2017). The last row lists the diagnosed  $c_d$  and  $c_a$  values for the annual cycle in the Faulk et al. (2017) Earth-like simulation.

that incorporates vertical advection of angular momentum:

$$\text{Ro}_{\text{gen}} \equiv \frac{1}{f} \left[ -\zeta + \frac{\omega}{v} \frac{\partial u}{\partial p} \right], \quad (17)$$

where  $v$  is meridional velocity,  $\omega$  is vertical velocity in pressure coordinates,  $p$  is pressure, and all quantities are zonal averages. This accounts for the considerable tilting of streamlines in the upper branch of the cross-equatorial cells [c.f. Fig. 3,4 of Faulk et al. (2017), Fig. 7 of Singh (2019), and Fig. 5 of (Hill et al. 2021)], which causes the conventional  $\text{Ro}$  to deviate from unity even if streamlines and angular momentum contours are everywhere parallel. Though it is the conventional  $\text{Ro}$  that appears in  $u_{\text{Ro}}$  and thus ultimately our expressions for  $\varphi_d$ , for the simulations we argue that (17) is more instructive: for the two-layer model of baroclinic instability utilized, the bulk upper-tropospheric behavior is more relevant than that at any chosen pressure level. And as streamlines begin tilting toward the surface in the descending branch, the conventional  $\text{Ro}$  at any given level decreases, while the bulk zonal velocities of the upper branch still roughly correspond to the planetary angular momentum values from where the streamlines exited the boundary layer in the ascending branch. In other words, along streamlines angular momentum is nearly conserved (see Fig. 7 of Singh (2019)), which the meridional profile of  $\text{Ro}$  at a fixed pressure level cannot capture.

The generalized Rossby number is close to unity over a large fraction of the cross-equatorial Hadley cell extent in all cases. (Both forms are masked out near the equator, as specified in the caption, where division by the Coriolis parameter makes them less physically meaningful.) The difference made by the vertical advection term is particularly large in the ascending branches. For either version, we subjectively identify two regimes over the descending branch. Slowly rotating cases have  $\text{Ro}_{\text{gen}}$  relatively uniform or even increasing slightly from the equator to the

winter descending edge. More rapidly rotating cases have  $\text{Ro}_{\text{gen}}$  decreasing poleward, approaching zero in the vicinity of the winter descending edge, but there is considerable scatter in the value of  $\text{Ro}_{\text{gen}}$  at the edge. Despite this variation in the Rossby number across the simulations, it is evidently small enough that taking the bulk  $\text{Ro}_{\text{gen}}$  value as fixed in our scalings does not introduce major error.

## 5. Conclusions

### a. Summary

We have introduced a unified theory for the latitudes of all three Hadley cell edges—the equatorward, ascending edge ( $\varphi_a$ ) shared by the two Hadley cells as well as each cell’s poleward, descending edge ( $\varphi_d$ )—throughout the annual cycle by combining two previous theories. First we predict  $\varphi_a$  using our recent theory based on the meridional extent of low-latitude supercritical forcing (Hill et al. 2021). We then essentially plug this  $\varphi_a$  into the theory for  $\varphi_d$  based on baroclinic instability onset of Kang and Lu (2012) that uses the seasonally varying  $\varphi_a$  and an assumed uniform Rossby number ( $\text{Ro}$ ) within each Hadley cell’s upper branch. The new theory predicts that  $\varphi_d$  is displaced poleward when  $\text{Ro}$  decreases or as  $\varphi_a$  moves poleward, and  $\varphi_a$  varies with the thermal Rossby number ( $\text{Ro}_{\text{th}}$ ) to the one-third power. But in the small-angle limit reasonable for Earth, the dependence on  $\varphi_a$  drops out and the scaling for  $\varphi_d$  predicts a one-fourth power dependence on the planetary Burger number, or equivalently on  $\text{Ro}_{\text{th}}$  if only the planetary rotation rate (or any other term appearing in both  $\text{Bu}$  and  $\text{Ro}_{\text{th}}$ ) are varied. The mixed layer’s thermal inertia acts to damp and delay  $\varphi_a$  relative to the insolation annual cycle, which we account for via an “effective” forcing annual cycle based on the formalism of Mitchell et al. (2014).

In an Earth-like, seasonally forced idealized aquaplanet simulation with a relatively shallow, 10-m mixed layer

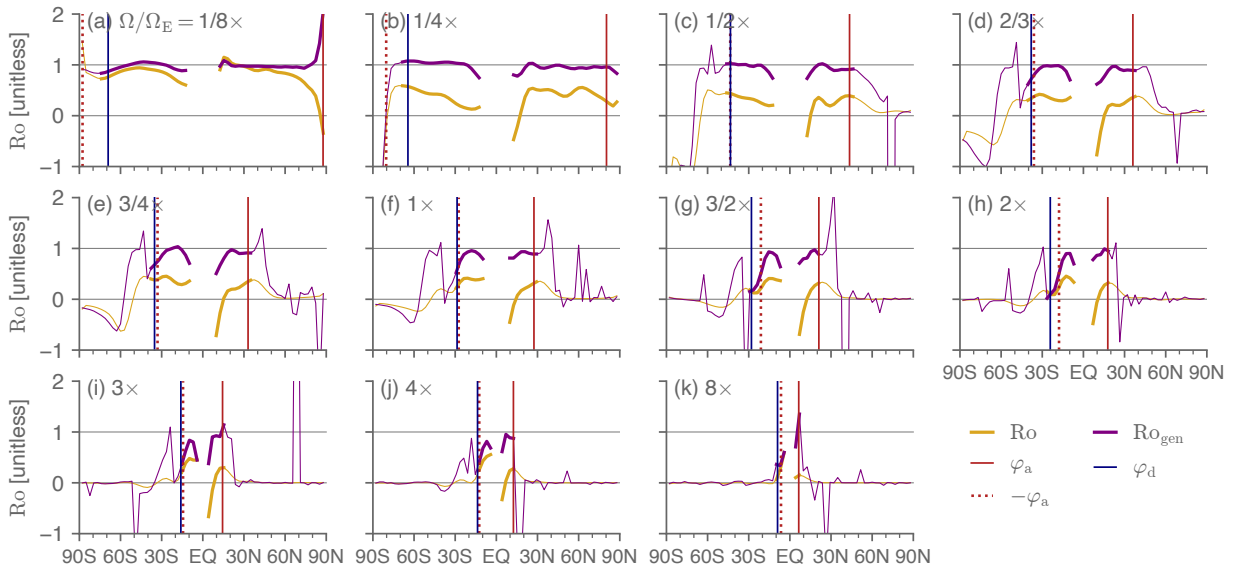


FIG. 5. Rossby number in the Singh (2019) simulations at the 300 hPa level, computed either conventionally using (3) or the generalized form (17) that accounts for the tilting of streamlines. Overlaid are the cell edges  $\varphi_a$  and  $\varphi_d$ , with  $-\varphi_a$  also shown to ease comparison of the relative poleward extents of  $\varphi_a$  and  $\varphi_d$ . Rossby number values outside of the Hadley circulation are shown as thinner curves, since they are less relevant. They are also masked near the equator where division by the Coriolis parameter makes them less meaningful, within  $12^\circ$  on either side for the slowest rotation rate and by  $1^\circ$  less on either side for each subsequent rotation rate.

ocean depth,  $\varphi_a$  migrates rapidly to  $\sim 25^\circ$  into either summer hemisphere, and this seasonal cycle is well captured by the supercriticality-based scaling. The summer cell is too weak for the summer  $\varphi_d$  to be meaningful, but the winter  $\varphi_d$  varies by only  $\lesssim 5^\circ$  latitude about its mean position in either hemisphere. Our combined theory predicting  $\varphi_a$  and  $\varphi_d$  captures this behavior with Ro kept at unity as in the original H00 model, but requires in place of Ro variations that the  $\varphi_d$  prediction be lagged by one month from that of  $\varphi_a$ —which in turn is lagged by  $\sim 1.5$  month from the insolation.

In simulations across a wide range of planetary rotation rates in three idealized GCMs, both  $\varphi_d$  and  $\varphi_a$  adhere to the respective power-law exponents predicted by our theory in the relevant small thermal Rossby number regime. This, combined with a smaller proportionality constant for  $\varphi_d$  compared to  $\varphi_a$ , helps explain why at very slow rotation rates the solstitial Hadley cell ascends essentially at the summer pole but descends considerably equatorward of the winter pole,  $\sim 70^\circ$ , rather than being roughly symmetric in extent about the equator as for more rapidly rotating cases including Earth.

## b. Discussion

How might a predictive theory for Ro be constructed? Hoskins et al. (2020) offer an intriguing perspective relating to the frequency of deep convection in the ascending

branch. They argue that only when convection is sufficiently deep will there be upper-tropospheric meridional outflow that travels nearly inviscidly (i.e. with  $Ro \approx 1$ ) toward either pole; at times and longitudes where deep convection is absent, they argue  $Ro \approx 0$ . Under those conditions, the time-mean, zonal-mean Ro field becomes a function of the spatial and temporal occurrence of deep convection in the ascending branch. This contrasts with the conventional, extratropically focused approach to Ro, wherein it is controlled by stresses from subtropical and extratropical eddies propagating into the deep tropics and breaking (Walker and Schneider 2006; Schneider 2006).

Vallis et al. (2015) speculate that Rossby waves are generated at the latitude of baroclinic instability onset, that these Rossby waves then propagate equatorward and break, and that the Hadley cell terminates at this wave-breaking latitude rather than the instability onset latitude. This equatorward displacement may relate to our need for the  $c_d < 1$  parameter value to fit the  $\varphi_d$  annual cycle in the seasonally forced aquaplanet simulation. And this additional step—with some finite timescale required for the overall process of Rossby wave development, propagation, and breaking—could contribute to the lag of  $\varphi_d$  relative to  $\varphi_a$  in the Earth-like seasonal cycle simulation. At the same time, across rotation rates the best fit  $c_d$  parameters exceed unity in some cases (Table 1), which is harder to square with this Rossby wave-based mechanism of Vallis et al. (2015).

The physical credibility of the two-layer model’s critical shear criterion for baroclinic instability has been fairly questioned; a series of studies utilize a more comprehensive treatment of baroclinic instability to argue that  $\varphi_d$  occurs where the vertical extent of baroclinic eddies spans a sufficient fraction of the troposphere (Korty and Schneider 2008; Levine and Schneider 2011, 2015). The same studies also incorporate the influence of moisture on the effective static stability  $\Delta_v$  (Levine and Schneider 2011, 2015).

Though we have relied on Ro being uniform over the upper branch of each Hadley cell (c.f. KL12), the baroclinic instability criterion is computed latitude-by-latitude, and as such strictly speaking the behavior of Ro equatorward of the instability onset latitude is irrelevant. This contrasts with the equal-area model appropriate for axisymmetric atmospheres, which depends on the meridional integral of the difference between the RCE and dynamically equilibrated potential temperature fields over the expanse of the cell. In principle one could solve the equal-area model with our fixed-Ro temperature field (6) as a means of indirectly introducing eddy influences into it.

Under annual-mean forcing in two dry and one moist idealized GCM, Mitchell and Hill (2021) find that  $\varphi_d$  scales as  $\Omega^{-1/3}$  in all three models. This could be squared with our  $\Omega^{-1/4}$  scaling for  $\varphi_a = 0$  if Ro scales as  $\Omega^{-2/3}$ . By eye from their Fig. 8 and 10, Ro does indeed follow an exponent close to this in two of the models—the same dry GCM we use and the moist GCM used by Faulk et al. (2017). But a simpler dry dynamical core (Held and Suarez 1994) shows no clear dependence of Ro on  $\Omega$ . Mitchell and Hill (2021) also put forward an “omega governor” mechanism which operates in the case that static stability and the effective heating (diabatic plus eddy heat convergence) averaged over the descending branch do not change. Under those conditions, the poleward extent and mass overturning rate of the Hadley cell must vary in tandem: the cell weakens if it narrows, and it widens if it strengthens. Prior to any adjustment by  $\varphi_d$ , if  $\varphi_a$  moves poleward then the cell widens, which under the omega governor would act to strengthen the overturning. One can imagine that strengthening causing Ro to increase, insofar as parcels then traverse the upper branch more rapidly and hence are less exposed to eddy stresses. The increase in Ro would, all else equal, act to move  $\varphi_d$  equatorward, countering the direct influence of  $\varphi_a$  moving poleward. (This apparently is not important for the annual cycle simulation discussed above where Ro = 1 throughout the annual cycle perform suitably.)

The Mitchell et al. (2014) model we use for the effective forcing annual cycle in the presence of thermal inertia is based on radiative equilibrium rather than RCE. It also considers only the equilibration of the ocean surface mixed layer rather than the coupled near-surface atmosphere-ocean. Cronin and Emanuel (2013) derive expressions for the timescale of equilibration to the RCE state in a coupled

ocean-atmosphere column but do not consider the latitudinally nor seasonally varying problem. It could be useful to combine these approaches, ideally arriving at an analytical model for the effective seasonally varying forcing for moist atmospheres.

Our theory could be further tested in numerous ways: against reanalysis data for the climatological annual cycle of the Hadley cells, against reanalysis data for inter-annual variability and trends, against comprehensive climate model simulations of global warming (c.f. KL12), and against simulations of other terrestrial planetary atmospheres. For the global warming problem, a useful starting point would be diagnosing seasonal, climatological best-fit Ro and  $\varphi_a$  values for each Hadley cell across comprehensive GCMs in preindustrial simulations in the CMIP6 archive. These could then be compared to diagnosed  $\varphi_d$  climatological values in the same simulations and forced changes in CMIP6 simulations under increased CO<sub>2</sub>, although care must be taken in interpreting e.g. changes in  $\Delta_h$ , which is strictly a parameter of the hypothetical latitude-by-latitude RCE state, not the dynamically equilibrated state that the archived simulations represent. We look forward to such tests.

**Acknowledgments.** We are grateful to Sean Faulk and Martin Singh for sharing the data from their simulations and for many valuable discussions. We thank Ilai Guendelman and three anonymous reviewers for helpful comments. S.A.H. acknowledges financial support from NSF Award 1624740 and from the Monsoon Mission, Earth System Science Organization, Ministry of Earth Sciences, Government of India. J.L.M. acknowledges funding from the Climate and Large-scale Dynamics program of the NSF, Award 1912673.

**Data availability statement.** Data from the Singh (2019) simulations is available for download at Singh (2021). Data from the Faulk et al. (2017) simulations is available for download at Faulk (2021). Data from the Hill et al. (2021) simulations is available for download at Hill (2021).

## References

- Adam, O., T. Bischoff, and T. Schneider, 2016: Seasonal and Inter-annual Variations of the Energy Flux Equator and ITCZ. Part I: Zonally Averaged ITCZ Position. *J. Climate*, **29** (9), 3219–3230, <https://doi.org/10.1175/JCLI-D-15-0512.1>.
- Becker, E., G. Schmitz, and R. Geprags, 1997: The feedback of midlatitude waves onto the Hadley cell in a simple general circulation model. *Tellus A*, **49** (2), 182–199, <https://doi.org/10.1034/j.1600-0870.1997.t01-1-00003.x>.
- Bordoni, S., and T. Schneider, 2008: Monsoons as eddy-mediated regime transitions of the tropical overturning circulation. *Nature Geosci*, **1** (8), 515–519, <https://doi.org/10.1038/ngeo248>.
- Byrne, M. P., and R. Thomas, 2019: Dynamics of ITCZ Width: Ekman Processes, Non-Ekman Processes, and Links to Sea Surface

- Temperature. *J. Atmos. Sci.*, **76** (9), 2869–2884, <https://doi.org/10.1175/JAS-D-19-0013.1>.
- Caballero, R., R. T. Pierrehumbert, and J. L. Mitchell, 2008: Axisymmetric, nearly inviscid circulations in non-condensing radiative-convective atmospheres. *Q.J.R. Meteorol. Soc.*, **134** (634), 1269–1285, <https://doi.org/10.1002/qj.271>.
- Cronin, T. W., and K. A. Emanuel, 2013: The climate time scale in the approach to radiative-convective equilibrium. *Journal of Advances in Modeling Earth Systems*, **5** (4), 843–849, <https://doi.org/10.1002/jame.20049>.
- Davis, N. A., and T. Birner, 2022: Eddy-Mediated Hadley Cell Expansion due to Axisymmetric Angular Momentum Adjustment to Greenhouse Gas Forcings. *Journal of the Atmospheric Sciences*, **79** (1), 141–159, <https://doi.org/10.1175/JAS-D-20-0149.1>.
- Dima, I. M., and J. M. Wallace, 2003: On the Seasonality of the Hadley Cell. *J. Atmos. Sci.*, **60** (12), 1522–1527, [https://doi.org/10.1175/1520-0469\(2003\)060<1522:OTSOTH>2.0.CO;2](https://doi.org/10.1175/1520-0469(2003)060<1522:OTSOTH>2.0.CO;2).
- Donohoe, A., D. M. W. Frierson, and D. S. Battisti, 2014: The effect of ocean mixed layer depth on climate in slab ocean aquaplanet experiments. *Clim Dyn*, **43** (3–4), 1041–1055, <https://doi.org/10.1007/s00382-013-1843-4>.
- Emanuel, K. A., 1995: On thermally direct circulations in moist atmospheres. *J. Atmos. Sci.*, **52** (9), 1529–1534, [https://doi.org/10.1175/1520-0469\(1995\)052<1529:OTDCIM>2.0.CO;2](https://doi.org/10.1175/1520-0469(1995)052<1529:OTDCIM>2.0.CO;2).
- Faulk, S., 2021: Output from the Faulk, Bordoni, and Mitchell 2017 J. Atmos. Sci. idealized aquaplanet simulations. Zenodo, <https://doi.org/10.5281/ZENODO.5796259>.
- Faulk, S., J. Mitchell, and S. Bordoni, 2017: Effects of rotation rate and seasonal forcing on the ITCZ extent in planetary atmospheres. *J. Atmos. Sci.*, **74** (3), 665–678, <https://doi.org/10.1175/JAS-D-16-0014.1>.
- Frierson, D. M. W., I. M. Held, and P. Zurita-Gotor, 2006: A gray-radiation aquaplanet moist GCM. Part I: Static stability and eddy scale. *J. Atmos. Sci.*, **63** (10), 2548–2566, <https://doi.org/10.1175/JAS3753.1>.
- Guendelman, I., and Y. Kaspi, 2018: An Axisymmetric Limit for the Width of the Hadley Cell on Planets With Large Obliquity and Long Seasonality. *Geophysical Research Letters*, **45** (24), 13,213–13,221, <https://doi.org/10.1029/2018GL080752>.
- Guendelman, I., and Y. Kaspi, 2019: Atmospheric Dynamics on Terrestrial Planets: The Seasonal Response to Changes in Orbital, Rotational, and Radiative Timescales. *ApJ*, **881** (1), 67, <https://doi.org/10.3847/1538-4357/ab2a06>.
- Guendelman, I., and Y. Kaspi, 2020: Atmospheric Dynamics on Terrestrial Planets with Eccentric Orbits. *ApJ*, **901** (1), 46, <https://doi.org/10.3847/1538-4357/abae8>.
- Held, I. M., 2000: The General Circulation of the Atmosphere. *The General Circulation of the Atmosphere: 2000 Program in Geophysical Fluid Dynamics*, No. WHOI-2001-03, Woods Hole Oceanog. Inst. Tech. Rept., Woods Hole Oceanographic Institution, 1–54.
- Held, I. M., and A. Y. Hou, 1980: Nonlinear axially symmetric circulations in a nearly inviscid atmosphere. *J. Atmos. Sci.*, **37** (3), 515–533, [https://doi.org/10.1175/1520-0469\(1980\)037<0515:NASCIA>2.0.CO;2](https://doi.org/10.1175/1520-0469(1980)037<0515:NASCIA>2.0.CO;2).
- Held, I. M., and M. J. Suarez, 1994: A Proposal for the Intercomparison of the Dynamical Cores of Atmospheric General Circulation Models. *Bull. Amer. Meteor. Soc.*, **75** (10), 1825–1830, [https://doi.org/10.1175/1520-0477\(1994\)075<1825:APFTIO>2.0.CO;2](https://doi.org/10.1175/1520-0477(1994)075<1825:APFTIO>2.0.CO;2).
- Hilgenbrink, C. C., and D. L. Hartmann, 2018: The Response of Hadley Circulation Extent to an Idealized Representation of Poleward Ocean Heat Transport in an Aquaplanet GCM. *J. Climate*, **31** (23), 9753–9770, <https://doi.org/10.1175/JCLI-D-18-0324.1>.
- Hill, S., 2021: Output of dry idealized GCM simulations under perpetual solstice-like forcing. Zenodo, <https://doi.org/10.5281/ZENODO.5796233>.
- Hill, S. A., S. Bordoni, and J. L. Mitchell, 2019: Axisymmetric constraints on cross-equatorial Hadley Cell extent. *J. Atmos. Sci.*, **76** (6), 1547–1564, <https://doi.org/10.1175/JAS-D-18-0306.1>.
- Hill, S. A., S. Bordoni, and J. L. Mitchell, 2020: Axisymmetric Hadley Cell theory with a fixed tropopause temperature rather than height. *J. Atmos. Sci.*, **77** (4), 1279–1294, <https://doi.org/10.1175/JAS-D-19-0169.1>.
- Hill, S. A., S. Bordoni, and J. L. Mitchell, 2021: Solstitial Hadley Cell Ascending Edge Theory from Supercriticality. *Journal of the Atmospheric Sciences*, **78** (6), 1999–2011, <https://doi.org/10.1175/JAS-D-20-0341.1>.
- Hoskins, B. J., G.-Y. Yang, and R. M. Fonseca, 2020: The detailed dynamics of the June–August Hadley Cell. *Quarterly Journal of the Royal Meteorological Society*, **n/a** (n/a), <https://doi.org/10.1002/qj.3702>.
- Kang, S. M., and J. Lu, 2012: Expansion of the Hadley Cell under global warming: Winter versus summer. *J. Climate*, **25** (24), 8387–8393, <https://doi.org/10.1175/JCLI-D-12-00323.1>.
- Korty, R. L., and T. Schneider, 2008: Extent of Hadley circulations in dry atmospheres. *Geophys. Res. Lett.*, **35** (23), L23 803, <https://doi.org/10.1029/2008GL035847>.
- Lee, H.-I., and J. L. Mitchell, 2021: The Dynamics of Quasi-Stationary Atmospheric Rivers and Their Implications for Monsoon Onset. *Journal of the Atmospheric Sciences*, **78** (8), 2353–2365, <https://doi.org/10.1175/JAS-D-20-0262.1>.
- Levine, X. J., and T. Schneider, 2011: Response of the Hadley Circulation to Climate Change in an Aquaplanet GCM Coupled to a Simple Representation of Ocean Heat Transport. *Journal of the Atmospheric Sciences*, **68** (4), 769–783, <https://doi.org/10.1175/2010JAS3553.1>.
- Levine, X. J., and T. Schneider, 2015: Baroclinic Eddies and the Extent of the Hadley Circulation: An Idealized GCM Study. *J. Atmos. Sci.*, **72** (7), 2744–2761, <https://doi.org/10.1175/JAS-D-14-0152.1>.
- Lindzen, R. S., and A. V. Hou, 1988: Hadley circulations for zonally averaged heating centered off the equator. *J. Atmos. Sci.*, **45** (17), 2416–2427, [https://doi.org/10.1175/1520-0469\(1988\)045<2416:HCFZAH>2.0.CO;2](https://doi.org/10.1175/1520-0469(1988)045<2416:HCFZAH>2.0.CO;2).
- Mitchell, J. L., and S. A. Hill, 2021: Constraints from Invariant Subtropical Vertical Velocities on the Scalings of Hadley Cell Strength and Downdraft Width with Rotation Rate. *Journal of the Atmospheric Sciences*, **78** (5), 1445–1463, <https://doi.org/10.1175/JAS-D-20-0191.1>.
- Mitchell, J. L., G. K. Vallis, and S. F. Potter, 2014: Effects of the Seasonal Cycle on Superrotation in Planetary Atmospheres. *ApJ*, **787** (1), 23, <https://doi.org/10.1088/0004-637X/787/1/23>.

- O’Gorman, P. A., and T. Schneider, 2008: The hydrological cycle over a wide range of climates simulated with an idealized GCM. *J. Climate*, **21** (15), 3815–3832, <https://doi.org/10.1175/2007JCLI2065.1>.
- Plumb, R. A., and A. Y. Hou, 1992: The response of a zonally symmetric atmosphere to subtropical thermal forcing: Threshold behavior. *J. Atmos. Sci.*, **49** (19), 1790–1799, [https://doi.org/10.1175/1520-0469\(1992\)049<1790:TROAZS>2.0.CO;2](https://doi.org/10.1175/1520-0469(1992)049<1790:TROAZS>2.0.CO;2).
- Rodwell, M. J., and B. J. Hoskins, 1996: Monsoons and the dynamics of deserts. *Q.J.R. Meteorol. Soc.*, **122** (534), 1385–1404, <https://doi.org/10.1002/qj.49712253408>.
- Schneider, T., 2004: The tropopause and the thermal stratification in the extratropics of a dry atmosphere. *J. Atmos. Sci.*, **61** (12), 1317–1340, [https://doi.org/10.1175/1520-0469\(2004\)061<1317:TTATTS>2.0.CO;2](https://doi.org/10.1175/1520-0469(2004)061<1317:TTATTS>2.0.CO;2).
- Schneider, T., 2006: The general circulation of the atmosphere. *Annu. Rev. Earth Planet. Sci.*, **34**, 655–688.
- Schneider, T., and S. Bordoni, 2008: Eddy-Mediated Regime Transitions in the Seasonal Cycle of a Hadley Circulation and Implications for Monsoon Dynamics. *J. Atmos. Sci.*, **65** (3), 915–934, <https://doi.org/10.1175/2007JAS2415.1>.
- Singh, M., 2021: Output of aquaplanet idealized GCM simulations under perpetual solstice-like forcing from Singh 2019, *J. Atmos. Sci. Zenodo*, <https://doi.org/10.5281/ZENODO.5796278>.
- Singh, M. S., 2019: Limits on the extent of the solstitial Hadley Cell: The role of planetary rotation. *J. Atmos. Sci.*, **76** (7), 1989–2004, <https://doi.org/10.1175/JAS-D-18-0341.1>.
- Vallis, G. K., P. Zurita-Gotor, C. Cairns, and J. Kidston, 2015: Response of the large-scale structure of the atmosphere to global warming. *Q.J.R. Meteorol. Soc.*, **141** (690), 1479–1501, <https://doi.org/10.1002/qj.2456>.
- Walker, C. C., and T. Schneider, 2006: Eddy influences on Hadley circulations: Simulations with an idealized GCM. *J. Atmos. Sci.*, **63** (12), 3333–3350, <https://doi.org/10.1175/JAS3821.1>.
- Watt-Meyer, O., and D. M. W. Frierson, 2019: ITCZ Width Controls on Hadley Cell Extent and Eddy-Driven Jet Position and Their Response to Warming. *J. Climate*, **32** (4), 1151–1166, <https://doi.org/10.1175/JCLI-D-18-0434.1>.
- Wei, H.-H., and S. Bordoni, 2018: Energetic Constraints on the ITCZ Position in Idealized Simulations With a Seasonal Cycle. *Journal of Advances in Modeling Earth Systems*, **10** (7), 1708–1725, <https://doi.org/10.1029/2018MS001313>.
- Zurita-Gotor, P., and I. M. Held, 2018: The Finite-Amplitude Evolution of Mixed Kelvin–Rossby Wave Instability and Equatorial Superrotation in a Shallow-Water Model and an Idealized GCM. *J. Atmos. Sci.*, **75** (7), 2299–2316, <https://doi.org/10.1175/JAS-D-17-0386.1>.